applied sciences

Article

A Morphing Deployable Mechanism for Re-Entry Capsule Aeroshell

Ignazio Dimino [1,*], Cristian Vendittozzi [2], William Reis Silva [2], Salvatore Ameduri [3] and Antonio Concilio [4]

[1] Adaptive Structures Technologies, The Italian Aerospace Research Centre, Via Maiorise, 81043 Capua, Italy
[2] FGA (Faculdade do Gama), Universidade de Brasília, Gama 72444-240, Brazil
[3] Sensors and Actuators for Adaptive Structures, The Italian Aerospace Research Centre, CIRA, Via Maiorise, 81043 Capua, Italy
[4] Adaptive Structures Division, The Italian Aerospace Research Centre, CIRA, Via Maiorise, 81043 Capua, Italy
* Correspondence: i.dimino@cira.it; Tel.: +39-0823-623308

Abstract: Morphing technology is increasingly emerging as a novel and alternative approach for performing the controlled re-entry and precise landing of space vehicles by using adaptive aeroshell structure designs. This work is intended as a preliminary conceptual design of an innovative shape-changing mechanism for the controlled re-entry and safe recovery of CubeSat class systems aimed at recovering payloads and data from LEO at low cost for post flight inspections and experimentations. Such an adaptive and mechanically deployable aeroshell consists of a multi-hinge assembly based on a set of finger-like articulations having two-modal capabilities. The deployable surface can be modulated by a single translational actuator in order to adapt the lift-to-drag ratio for guided entry. Furthermore, once deployed, the system can activate eight small movable aerodynamic flaps that can be individually morphed via an SMA-based actuation to enhance the capsule maneuverability during the re-entry trajectory, by using exclusively aerodynamic forces to guarantee additional precision in landing. Multi-body simulations on retraction/deployment of the system are addressed to investigate the most critical aspects for actual implementation of the concept. Additionally, the morphing behavior and the control effect of the shape memory alloy actuation are preliminary assessed through parametric analysis. This paper is framed within a scientific cooperation between Italy and Brazil in the framework of the SPLASH project, funded in part for the Italian side by a grant from the Italian Ministry of Foreign Affairs and International Cooperation (MAECI), and by CONFAP through the involved State Funding Agencies (FAPs) for the Brazilian side.

Keywords: morphing aeroshell; smart materials; re-entry vehicles

check for updates

Citation: Dimino, I.; Vendittozzi, C.; Reis Silva, W.; Ameduri, S.; Concilio, A. A Morphing Deployable Mechanism for Re-Entry Capsule Aeroshell. *Appl. Sci.* **2023**, *13*, 2783. https://doi.org/10.3390/app13052783

Academic Editor: Maria Grazia De Giorgi

Received: 31 December 2022
Revised: 14 February 2023
Accepted: 16 February 2023
Published: 21 February 2023

1. Introduction

The demand for deployable re-entry systems that leverage and accommodate CubeSat or small satellites for high-speed entry at destinations with atmospheres has constantly increased in recent years [1–3]. A number of studies have proposed CubeSat design concepts that directly incorporate deployable de-orbit and re-entry modules within a standard form factor (1U–16U) to offer delivery capabilities for single CubeSats or constellations [4–6]. The related entry systems, known as mechanically-deployable or inflatable deployable systems, can be deployed via mechanisms or inflated once in space. Typically, mechanically deployed systems consist of ribs and struts supporting a mechanism that deploys a load-bearing flexible skin after launch [7]. Inflatable deployable systems use pressurized gases to inflate an aeroshell, which are also made of flexible thermal protection system (TPS) material [8].

Both aerocapture and entry, as well as descent and landing can be potentially performed by using a single re-entry system for science missions at planets. Several concepts of deployable aerodecelerators for satellite de-orbit and/or re-entry using flexible heat shields exist in the literature [9–11]. Additionally, various assessments have taken place by investigating aerodynamics and heating of flexible thermal protection systems that can deform under static and dynamic loads [12]. Due to the larger wetted area, both deployable and inflatable aeroshells ensure a lower ballistic coefficient, which is a non-dimensional ratio of the vehicle's entry mass to the product of the drag coefficient (CD) and the projected reference area, thus making it possible to fulfill the tight volumetric constraints imposed by the CubeSat platform. The ADEPT concept, developed by NASA [13,14], does integrate the entry system around standard CubeSat units in order to increase the volume/mass available for science payload. By expanding to a larger diameter prior to entry in order to increase drag, such a concept has shown to achieve a stowed diameter a factor of 3–4 times smaller than an equivalent rigid aeroshell, thus enabling higher entry performance suitable for a variety of planetary or earth high speed entries that require high temperature materials [15]. Similarly, a novel deployable Mars aeroshell concept consisting of thermal protection system (TPS) panels that are fitted between retractable ribs was developed at Imperial College London [16].

As well as enabling higher payload mass suitable for scientific instruments, morphing technology can provide mechanically deployable aeroshells with improved entry conditions than previous paradigms, suitable for the safe and timely recovery of payloads and samples in a desired landing site with reduced risks and costs [17,18]. Their potential ability to either globally or locally modulate the drag profile during re-entry operations by using flexible morphing heat shields offers considerable benefits over traditional rigid aeroshells including higher volume, mass and payload form factor, more accurate guidance trajectories, and improved landing accuracy by using aerodynamic drag. Additionally, lower peak decelerations, heat loads, and fluxes can be effectively achieved to protect the payload from the re-entry environment.

Prior work on drag modulation has proved the ability to guide a satellite to a desired re-entry interface point [19–22]. In ref. [23], the results show that aerodynamic drag modulation of umbrella-like heat shields is an efficient way to control the re-entry location. An adaptive aerobrake using aerodynamic flaps is also addressed in ref. [24] to efficiently steer the vehicle during re-entry. In ref. [25], such a technology is also combined with a fiber-optic-based closed-loop feedback monitoring system in order to realize a full autonomous re-entry system.

The overall context of this study is the first executive program for scientific and technological cooperation between Italy and Brazil, supporting joint research projects for the years 2022–2024 in priority research areas, including space science. This work is framed within the joint research project SPLASH (Self-DePloyable FLexible AeroSHell for de-Orbiting and Space Re-entry), funded by the Italian Ministry of Foreign Affairs and International Cooperation (MAECI) for the Italian side and by CONFAP for the Brazilian side. It brings together a consortium of internationally leading organizations in space engineering, coordinated by CIRA, to carry out research activities on an innovative mechanically deployable shape-changing re-entry aeroshell concept capable of achieving multiple target shapes enabling adaptive re-entry capabilities.

This paper describes the preliminary activities carried out by the international research team for the development of a novel re-entry concept featuring advanced mechanisms and shape memory alloy (SMA) actuation for the structural shape control of a re-entry aeroshell, with the aim of enabling adaptive entry trajectories with reduced landing dispersions. Unlike the ADEPT 3U or ADEPT 12U aeroshell concepts that integrate the entry system around the standard 3U or 12U CubeSat form factors, one of the key objectives for this study is to integrate the entire morphing concept within a standard 12U CubeSat deployer, as shown in Figure 1, in order to take advantage of existing CubeSat deployment systems. CubeSat dimensions and features are outlined in the CubeSat Specification Drawings [26,27]. The main design driver is, thus, used to expand the mechanism to a larger diameter by using a single translational actuator in order to protect the payload during entry and, once deployed, adapt the aeroshell shape by morphing flap segments via an SMA-based actuation. This paper will explore the motivation behind the concept and investigate some of the challenges facing the design of a morphing mechanism for re-entry system using smart materials.

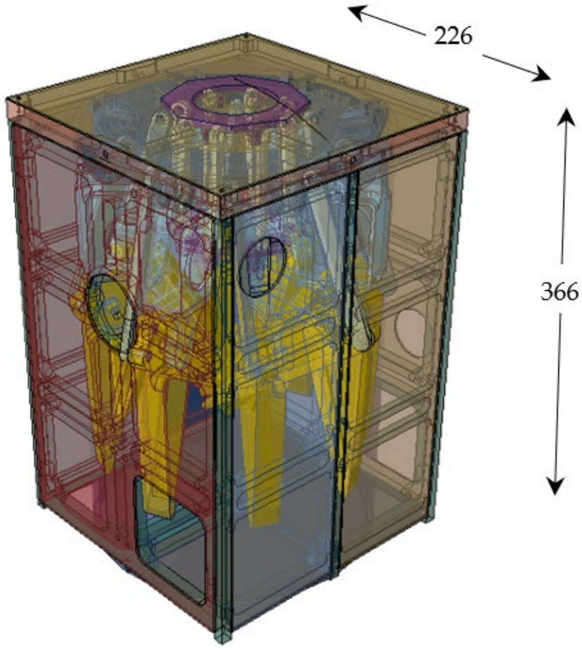

Figure 1. Preliminary SPLASH concept for 12U Cubesat Platform.

2. Re-Entry Mission from LEO

Mechanically deployed aeroshells can be deployed and retracted repeatably. Unlike rigid or inflatables decelerators, adaptive deployable concepts can provide controlled re-entry trajectories and enhanced flight maneuverability by integrating shape-morphing strategies into high temperature and flexible TPS.

The sample return mission has three main challenges: 1. Withstanding high temperatures during re-entry; 2. Steering the Cubesat during re-entry in order to follow a predefined trajectory; 3. Enabling high precision landing after passing through the atmosphere. The aim of this paper is to propose an initial idea of a low ballistic coefficient planetary entry system that incorporates an innovative shape-changing mechanism that can be housed in the folded configuration inside a 12U Cubesat and then deployed with the intent of a re-entry and landing for payload recovery. By considering an ISS payload as an example, scientific data can be recovered for post flight inspections and experimentations, opening new possibilities of samples to return from space with minimal or no propulsion systems.

As a very first approximation, a Newtonian approach is considered to estimate the spacecraft drag coefficient (CD) by simplifying its shape with a cone, as shown in Figure 2, by using the equation:

$$C_D = \left(1 - \sin^4 \delta_C\right)\left(\frac{r_n}{r_c}\right)^2 + 2\sin^2 \delta_C [1 - \left(\frac{r_n}{r_c}\right)^2 \cos^2 \delta_C] \quad (1)$$

where δ_C is the cone half angle, r_c is the cone base radius and r_n is the nose radius. A is the area of the frontal cross section, which is perpendicular to the motion direction.

A nominal undeflected "rigid" surface is preliminary considered to compute drag and ballistic coefficients for various cone half angles, as shown in Table 1. We can calculate also the ballistic coefficient (BC) for a target mass of 24 kg of the spacecraft:

$$\mathrm{BC} = \frac{\mathrm{m}}{\mathrm{AC_D}} \quad (2)$$

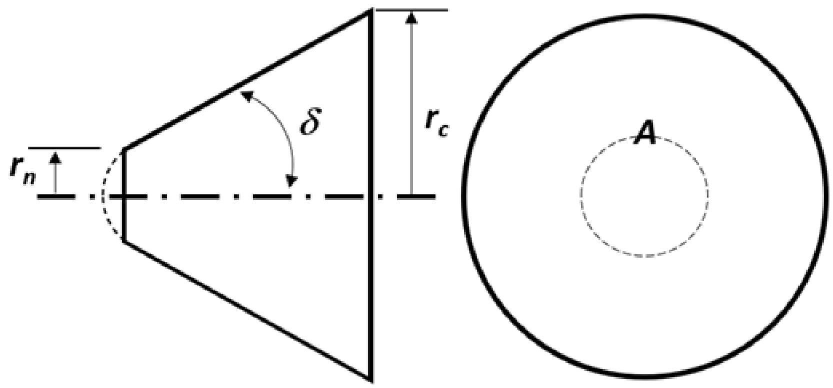

Figure 2. Example SPLASH concept configurations.

Table 1. Drag Coefficient (C_D) and Ballistic Coefficient (BC).

r_n (m)	0.108	0.108	0.108	0.108
r_c (m)	0.305	0.35878	0.419	0.488
m (kg)	24	24	24	24
A (m^2)	0.2923	0.40439	0.551	0.749
δ_C (deg)	15	30	45	60
C_D	0.243	0.551	1.017	1.503
BC (kg/m^2)	337.779	107.716	42.882	21.306

To calculate the heating rate ($\dot{q}$) we can use the formulas suggested by Tauber [28]:

$$\dot{q} = 1.83 \times 10^{-4} v^3 \sqrt{\frac{\rho}{r_{cn}}} \tag{3}$$

where v is the spacecraft velocity, r_{cn} is the curvature radius of the spacecraft nose, and ρ is the air density, which can be calculated according to the NRLMSIS atmosphere model. At 400 km, the density is about 2.42×10^{-12} kg/m^3, while at 120 km (reentry interface) the density is about 1.67×10^{-8} kg/m^3. The two heights represent the operational altitude of the satellite and the altitude defined as the reentry interface. The value of heating rate at the two altitudes can thus be estimated.

In case of active deorbiting, a Hohmann transfer is assumed at this preliminary stage between the two orbits at 400 and 120 km, respectively, in red and in green in Figure 3. In both cases, the orbits are circular (e = 0) and equatorial (I = 0). Table 2 summarizes the values of the circular velocities on the two orbits and the apogee and perigee velocities of the transfer orbit, as well as the Δvs required for the two transfers. After the second Δv, the CubeSat begins to spiral toward the ground, due to the increase in drag as atmospheric density increases.

Table 2. Orbits data.

$v_{c\text{-}400}$	7.669 km/s	Constant circular speed on the orbit at 400 km
$v_{c\text{-}120}$	7.832 km/s	Constant circular speed on the orbit at 120 km
Δv_1	−0.081 km/s	Δv required for moving from the first circular orbit to the Hohmann orbit.
Δv_2	−0.082 km/s	Δv required for moving from Hohmann's orbit to the second circular orbit.
Δv_{Tot}	0.163 km/s	Total Δv required for moving from the first to the second circular orbit.
T	2691.145 s	Transfer time along half Hohmann.

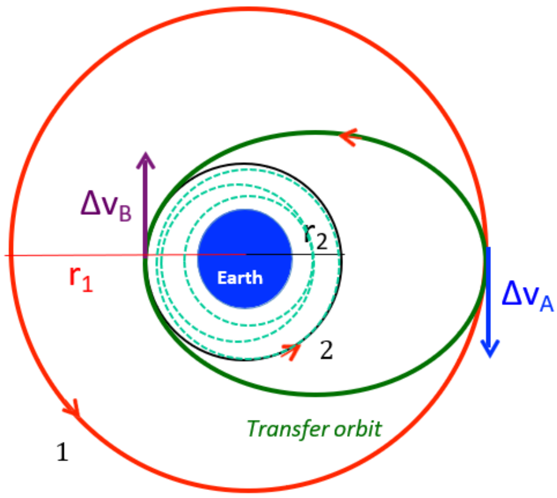

Figure 3. Hohmann Transfer.

The calculated heating rate on the CubeSat at 400 km is 3.30×10^2 W/m^2, while that at 120 km is 2.68×10^4 W/m^2. This helps in sizing both the flexible TPS and the underlying structural elements. Peak heat rate, total heat load, and peak dynamic pressure can thus be computed for different ballistic coefficients and used as a first approximation when performing mission concept sizing analysis. Such a preliminary analysis is based on our experience with the technology due to the insufficient knowledge on the morphing architecture until a first-loop design cycle has been completed. Figure 4 shows the simulation of the Hohman transfer; it is clearly visible how the spacecraft rapidly begins to decay after the first Δv performed at 400 km.

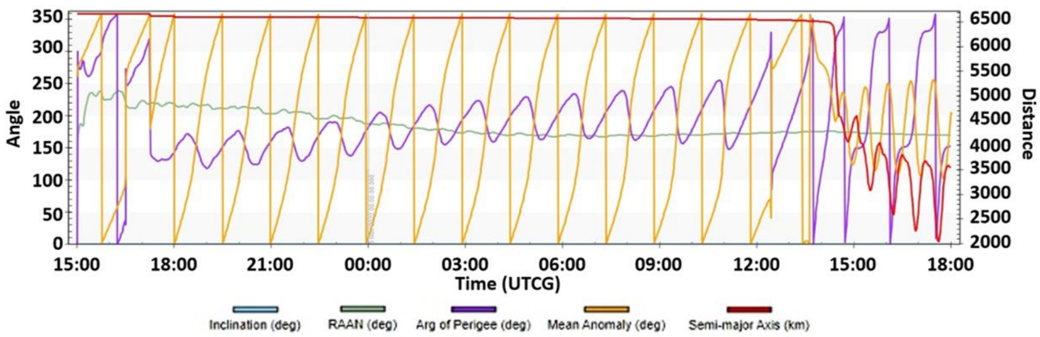

Figure 4. Simulation of Hohmann Transfer.

3. The Mechanically Deployable Morphing Aeroshell Concept

The proposed concept is an umbrella-like system consisting of structural ribs and struts that are covered by a flexible thermal protection system (TPS). Figure 5 shows a preliminary geometrical configuration. The capsule consists of a cylindrical structure containing all the subsystems necessary for the re-entry phase, including the adaptive mechanism and off-the-shelf ceramic fabrics for the deployable heat shield. The aeroshell uses a conical heat shield which is a proven, aerodynamically stable design. The structural skeleton consists of four primary components: nose cap, main body, ribs, and struts. The nose cap is designed to withstand thermal loads acting around the stagnation point. It acts as a conventional rigid component made of a ceramic matrix composite, possibly reinforced by ceramic fibers, for the best thermal insulation of the payload compartment. The TPS includes also a flexible high temperature material for the conical part of the heat shield. The "skin" is a light-weight high-performance fabric with great heat and flame protection capability, transferring also aerodynamic forces to the underlying ribs. The main body comprises a fixed ring and a moveable ring that support the main hinges of the morphing ribs and the actuation leverages, respectively. When the TPS is completely deployed, the base diameter of the two configurations is 0.8 m, while the cylindrical structure has a diameter of 21.6 cm.

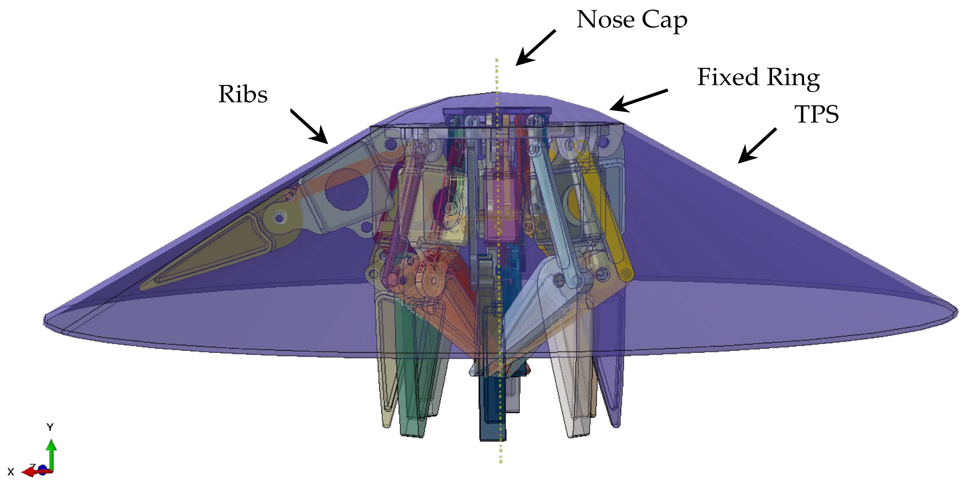

Figure 5. A general description of the aeroshell components.

System Configuration

The SPLASH structural skeleton is a multi-hinge assembly based on a set of finger-like articulations having two-modal capabilities:

- The deployable surface can be modulated by changing the sphere-cone angle in order to provide drag modulation capabilities, control the trajectory, and target the payload into the desired area for landing and recovery.
- Once deployed, the system can also activate eight small movable aerodynamic flaps that can be individually "morphed" to guarantee additional precision in landing that enhance the capsule's maneuverability during re-entry trajectory by using exclusively aerodynamic forces.

An actuated ring enables symmetrical rotation of the morphing ribs during deployment, as shown in Figure 6. Such a moveable ring is connected to the morphing ribs though eight actuation rods that drive the rotation of the main hinges of the ribs during system deployment/retraction. The whole mechanism is controlled by a screw-jack actuator guiding the position of the moveable ring.

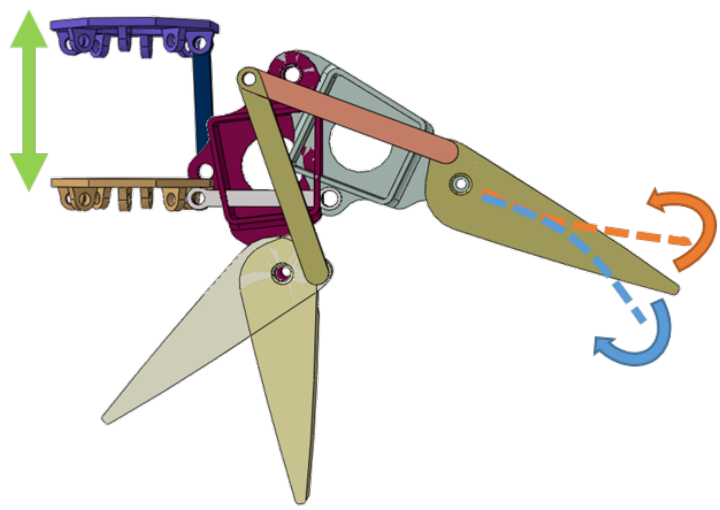

Figure 6. The deployment/retraction mechanism of the SPLASH concept for a single rib with morphing capabilities.

Each morphing rib consists of two consecutive blocks connected by a hinge, so that the resulting mechanism is forced to rotate according to specific gear ratio depending on the position of the inner linking beam connecting the outer block to the fixed ring. The resulting system, usually referred to as the finger-like mechanism [29], is thus of single-degree-of-freedom architecture (SDOF): if the rotation of any of the blocks is prevented, no change in shape can be obtained. On the contrary, if an actuator moves any of the blocks, all the other blocks follow the movement accordingly.

Additionally, when the deployable mechanism is locked in a given position, a shape memory alloy-based bending mechanism incorporated within the outer segments of the ribs will enable enhanced control capabilities during the re-entry trajectory by using active morphing flaps. The morphing mechanism is detailed in Section 5.

Shape Memory Alloys are selected as reference smart materials due to their compactness and high power/weight ratio [30]. They are particularly advantageous for space applications since they do not need external electronic sensors and control, as the shape change responsible for the actuation is an inherent material property. In the proposed application, when the SMA element is exposed to an increase in temperature, it undergoes a phase transformation that constitutes an actuator displacement for each SMA rod. Contraction by heating of the SMA actuators will deform the morphing flaps that will restore the initial shapes upon cooling. In the preliminary assessment, the operating range involves strain and stress limits of 8% and 700 MPa, respectively.

4. Multibody Simulations

In order to fully understand and predict the deployment behaviour of the assembly, a rigid multi-body simulation was set up in MSC/Adams. Each morphing rib was modelled as two rigid bodies connected by a revolute joint and a rigid link connected to the main body. The stowed configuration was optimized by envisaging a relative rotation between the two segments of the ribs. The system is shown in Figure 7.

Figure 7. Deployment of the morphing aeroshell as a function of the central actuation ring position.

Figure 8 outlines the variation in the main hinge angle of the ribs as the moveable ring deploys, where 0% corresponds to a stowed configuration and 100% corresponds to a fully deployed configuration. The system deploys symmetrically and a sphere–cone angle of about 60 degrees is reached by every rib. The system is then locked through a mechanical hard stop.

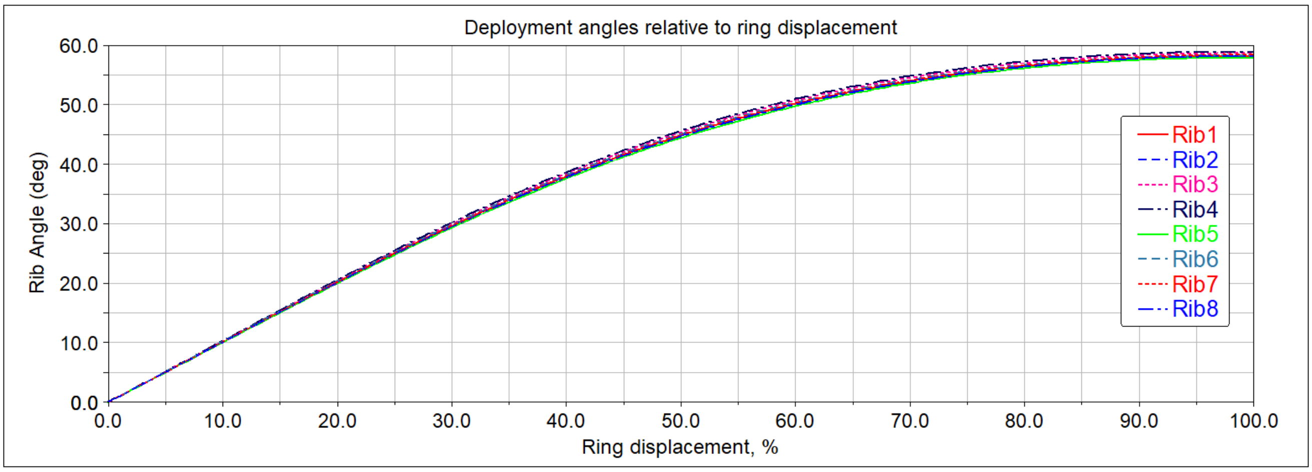

Figure 8. Deployment angles relative to ring displacement.

The deployment is fully controlled by the actuated ring, provided that each rib deploys symmetrically. It follows that the relative rotations between the rib segments with respect to the ring displacement will always remain the same for a given geometric case. Figure 9 shows how the two segments of a single morphing rib move relatively depending on the rate of deployment, up to the fully deployed configuration. The relative rotation is defined to be null (hinge angle = 0°) when the two rib segments are aligned. Then, it is considered to be negative when toward the inner part of the capsule, moving to the stowed position.

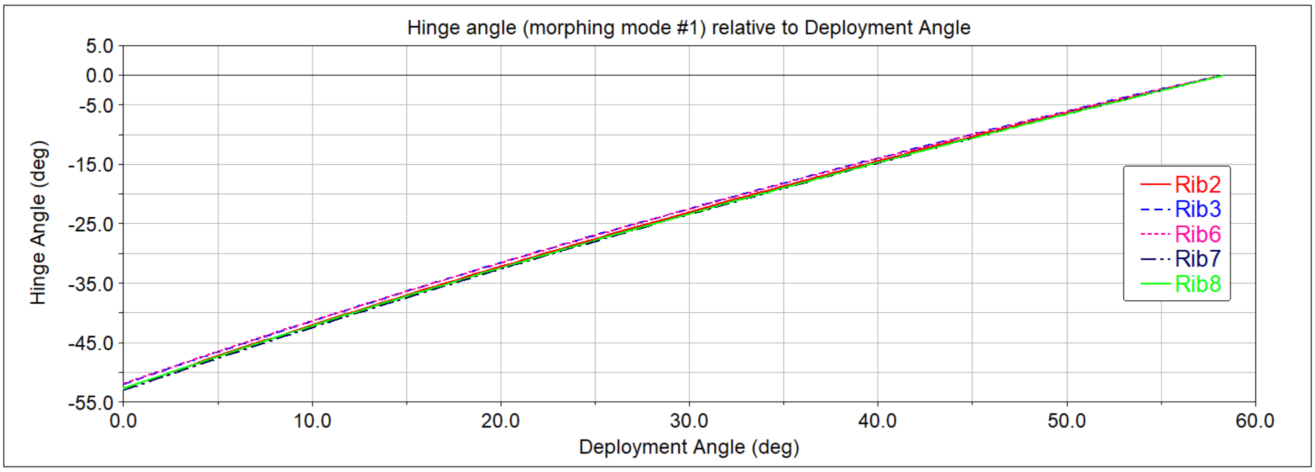

Figure 9. Variation in the relative rotations of the rib segments relative to deployment angle.

5. Morphing Tab Concept

5.1. SMA Modelling Approach

The structural morphing of the tabs is obtained through the SMA technology. The compactness, jointly to the relatively large energy density, makes this technology a good candidate for this specific steady (<1 Hz) application. This frequency upper limit is strictly related to thermal inertia of the material. In principle, the higher is the power supply, the shorter is the time of activation, and the more efficient is the cooling of the shorter in the de-activation phase. Many works can be found in the literature dealing with the speed of actuation of the SMA material and with strategies aimed at increasing it. A key role is played by the surface of the actuator, being strictly related to the heat transfer. To cite some examples, one recalls the work of Song et al. [31], focusing on an SMA-based actuator arriving at a frequency of 35 Hz; in this work, the strategy to overcome the above-mentioned upper limitation of 1 Hz is presented. In another work [32], S Sunjai Nakshatharan et al. investigated the effect of pre-stress on the actuation speed of an antagonistic SMA system and demonstrated the capability of achieving cyclic actuation in a period of 0.5 s.

Another critical aspect is the environmental temperature variation that impacts on needed power, time of activation and de-activation, and is, potentially, responsible for undesired activations. The starting activation temperature is kept generally over the upper limit of the operational scenario to avoid undesired activation. Designers can play on two parameters to control the activation temperature: the composition of the alloy and the preload level, the former assuring a wide excursion window for the transformation temperatures (more than one hundred of Celsius degrees), the latter causing an increase in the original activation temperatures regulated by the alloy transformation temperature/stress ratio.

To guarantee both inwards and outwards deflections, the antagonistic configuration, shown in Figure 10, was investigated. The original tab, illustrated in the sketch on the left, was milled preserving the root hinge region and the tip while shaping a flat middle plate on most of the chord. Root and tip were then linked to two SMA rods, as illustrated in the scheme on the right.

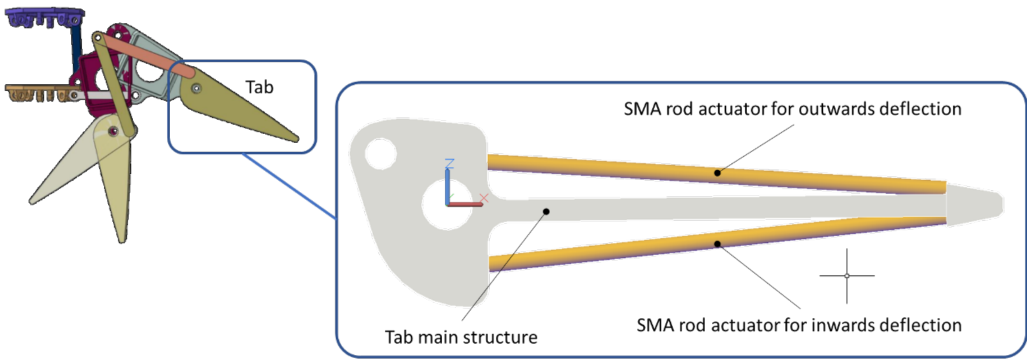

Figure 10. Architecture of the SMA morphable tab.

Two SMA rods were connected to the tip of the inner bending beams in an antagonistic way to provide both upward and downward deflections of the flaps. The contraction of one SMA actuator upon heating resulted in the extension of the opposing SMA actuator mechanically. Then, the contraction by heating of the extended actuator will reverse the actuation.

The SMA rods were mounted with a certain pre-stress to have enough martensite phase exploitable for the actuation, that is to say, potentially transformable by heating into austenite to produce strain recovery at a macroscopic level. When outwards deflection is required, the upper SMA is heated; its contraction thus causes the upwards movement of the tip. In the same way, when inwards deflection is required, the lower SMA is activated. Although it is possible to imagine the activation of an SMA rod when the other one is still warm and in austenite phase, in this work, only the case of the activation of an SMA when the other one is cold and in martensite phase was considered.

The main tab structure is prone only to deflections occurring in the plane containing the SMA elements; no constraint enforces this type of motion other than the geometry of the cross section of the main tab whose lowest inertia moment drives the planar deflection. To model the system, the non-linear MSC/Nastran SOL400 solver was used in combination with an SMA dedicated card, collecting all the information for the alloy constitutive law (austenite, martensite elastic modulus, Poisson ratio, transformation stresses at reference temperature, maximum recoverable strain, material density, transformation stress/temperature gradients). The data collected in Table 3 were used for the simulation and hereafter presented. A non-linear static analysis was implemented to simulate the different working steps of the SMA (pre-stretching and connection to the structure, upward activation, reverse to neutral position, downward activation, reverse to neutral position). A uniform incremental temperature load was assigned to the SMA material, passing from the initial value to the final one foreseen, per each step of the simulation.

Table 3. Material features used for the simulation.

Component	Parameter	Value
SMA rods	Austenite, Martensite elastic modulus	25 GPa, 10 GPa
	Austenite, Martensite Poisson ratio	0.33
	Density	6500 kg/m^3
	Max recoverable strain	0.023
	Martensite start and finish transformation stresses at 25 °C	150 MPa, 325 MPa
	Austenite start and finish transformation stresses at 25 °C	175 MPa, 45 MPa
	Stress/strain gradients for forward and rearward phase transformations	6.8 MPa/°C, 7.6 MPa/°C
Tab	Steel elastic modulus	210 GPa
	Steel Poisson ratio	0.32
	Density	7700 kg/m^3

The finite element model shown in Figure 11 was realized. The root region was not modelled; in fact, being remarkably more rigid than the other parts, it was replaced by constraints. The flat plate was simulated through beam elements. For the two SMA rods, hexahedral parabolic elements were considered; solid non-linear elements are, in fact, mandatory for the implementation of the SMA constitutive law. Finally, the tip was simulated through rigid connections among the edges of the SMA rods and the flat plate.

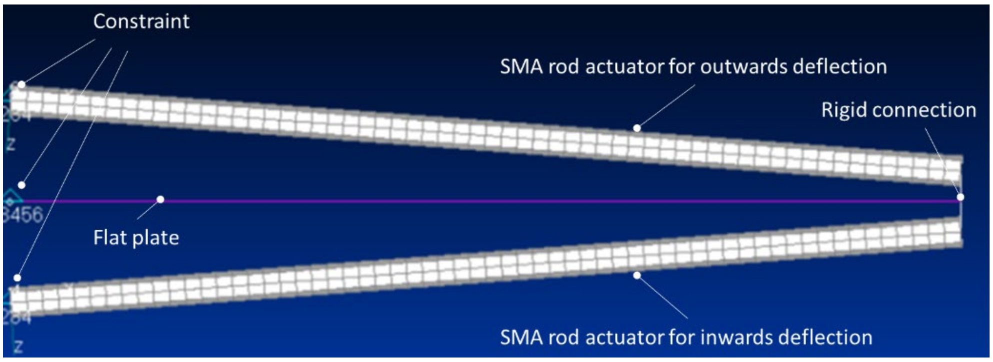

Figure 11. Finite element model of the SMA morphable tab.

Three moments of the life of the system were simulated:

- Integration of the SMA rods.
- Activation/heating of the upper SMA and then restoring/cooling into the neutral configuration.
- Activation/heating of the lower SMA and then restoring/cooling into the neutral configuration.

The integration of the SMA rods, originally in the austenite phase, consists of clamping the SMAs at the root region and stretching them up to bring the edges at the tip connection. During this operation, the applied load causes martensite production. Displacements along the rod axes were imposed during the simulation; as the edges coincided with the tip rigid connection, multiple constraints were imposed to pin the overlapping nodes. Then, the edges of the SMA were released to allow their elastic recovery and to achieve equilibrium with the tab structure. In Figure 12, the initial configuration (SMA before stretching) and the fully integrated configuration (SMA stretched, connected, and in equilibrium with the flat plate) are illustrated.

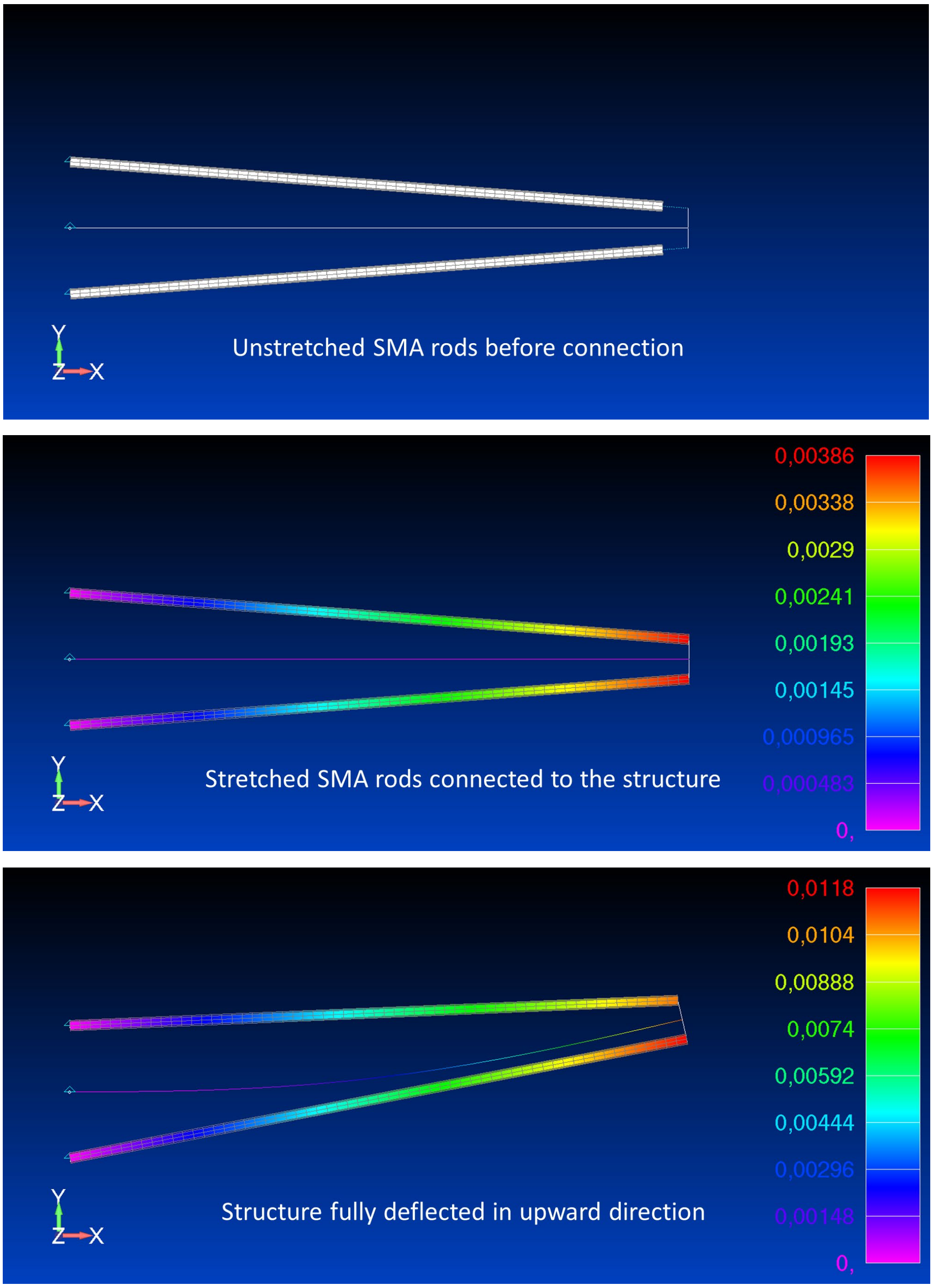

Figure 12. Integration simulation steps: SMA rods before stretching (**top**), connected to the flat plate (**middle**), and fully upward deflected (**bottom**).

The stress level within the components was assumed as design constraint. 1/3 of the ultimate stress was assumed as allowable for the structure material; the allowable arose to the 80% of the ultimate stress for the SMA material; this choice is justified by the necessity to exploit as much as possible the SMA actuation capability, strictly related to the amount of martensite generated during the pre-load. Another design constraint considered was represented by structural instability. The elastic recovery of the SMA rods in fact produces an axial force on the flat plate potentially causing its collapse. To prevent this event, the pre-load level of each SMA rod was assumed to be lower than 1/3 of the instability load of the flat plate. In this way, a margin of 33% was assumed also in view of the compressive action due to the stretched skin, currently not considered.

5.2. Parametrization and Results

On the basis of the model illustrated above, a parametric study was organized. The target was to maximize the deflection of the tip of the tab, meeting the requirements in terms of structural safety discussed in the previous section.

In Table 4, the parameters are considered, and their variation range are reported. The width of the plate was kept constant at 40 mm, while a maximum temperature of 500 °C was considered to guarantee full activation, even crossing the effective limit of complete conversion of the martensite. Despite the generally critical role played by the weight for aerospace applications, this parameter was not considered at this stage of the work. From one side, 16 SMA rods (each with a length of about 90 mm and a diameter no greater than 4 mm) scarcely contributed to the over-all weight (0.11 over 24 kg), and, from the other side, this additional parameter could have led astray the parameterization process with losses in terms of actuation performance.

Table 4. Parameters and ranges.

Parameter	Range
Flat plate thickness	1.8–2.2 mm
SMA rod diameter	1.35–1.65 mm
SMA initial length	81–99 mm

The morphing tab system was conceived to withstand the operational loads without the contribution of the SMA rods. In this sense, attention was paid to the action during the parameterization process due to the pre-stretching of the SMAs on the tab's main structures to prevent from any instability, even in fully deflected conditions.

Some considerations drove the selection of the mentioned parameters:

- The thickness of the plate increases the robustness of the structure but, at the same time, reduces the actuation performance.
- The SMA diameter increases its authority and reduces the stress level; however, large diameters may cause the collapse of the structure.
- Finally, the shorter the SMA the higher the stretching needed for the connection to the structure, with a, consequently, higher amount of martensite production and, thus, strain recoverability; however, large stretching causes higher stress levels within the SMA and greater transmitted forces, potentially causing the collapse of the flat plate.

A total of 125 configurations were simulated by considering 5 different values for each parameter. Only nine configurations met the safety requirements. They are compared in Figure 13 in terms of tip displacement, normalized with respect to the maximum one and its safety margins that are referred to the beam and the SMA material. The case/configuration 18 (red thick line), clearly enveloping all the others, was selected for this preliminary design. Its main features and performance are summarized in Tables 5 and 6, respectively.

Table 5. Optimal cases.

Parameter	Value
Flat plate thickness	1.8 mm
SMA rod diameter	1.58 mm
SMA initial length	90 mm

Table 6. Performance.

Parameter	Value
Tip displacement	10.9 mm
Beam Safety Margin	0.81
SMA Safety Margin	0.21

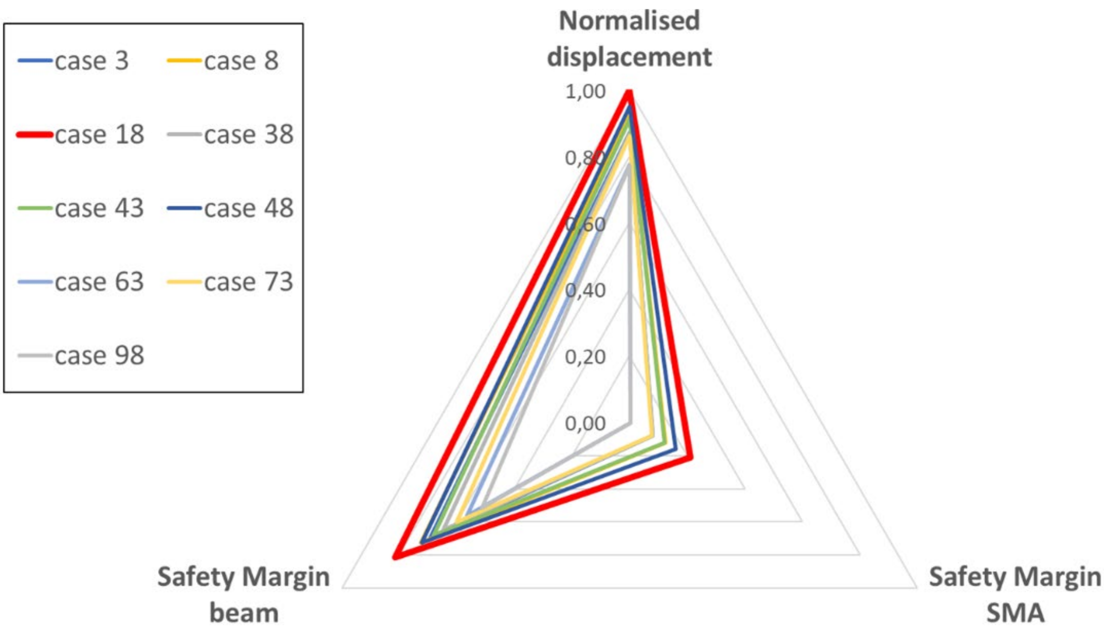

Figure 13. Comparison of the configurations meeting the safety requirements.

Then, the evolution of the displacement of the tip and the stress produced in the beam and in the SMA rods were computed and plotted in Figure 14 against the iteration step. The different phases were highlighted using different colors. The simulation started with the stretching of the SMA rods (yellow region); the beam was not affected by this operation, and thus both tip displacement and beam stress were zero. Then, the edges of the SMA rods were linked to the tip and released to enable elastic recovery (green region); no displacement of the tip occurs, owing to the symmetry of the loading, but the stress level rises in the beam and slightly decreases within the SMA rods. At the end of this phase, the upper SMA is heated (red region on the left); after having achieved the activation temperature threshold, the transformation starts, and the tip moves upwards until all the martensite is transformed into austenite (225 °C). At this point, even if the temperature further rises up to the imposed limit (500 °C), a plateau region is observed for the displacement and for the stress level of the beam and the SMA rods. It is also worth noting that, due to the presence of austenite, the stress level of the activated SMA is higher than the antagonistic. The cooling then starts (blue region on the left); the temperature of the SMA slows down to room temperature, and, as the transformation threshold is achieved, the plateau ends, and the displacement and the stress level quickly return to the neutral configuration. At this point, the activation and de-activation of the lower SMA starts; the same behavior was observed, as shown by the last two red and blue regions.

Finally, a rough estimate of the power consumption can be addressed. Assuming, per each SMA rod, a length of 90 cm, and considering a helicoid heater with a 2 mm square cable covering 50% of the SMA surface with 20 turns, a heating surface of 416 mm^2 can be obtained. Multiplying this latter value by a power per unit surface of 0.069 W/mm^2 needed by this type of heater [33], a power consumption of 28.7 W can be obtained. Considering an antagonistic actuation (only one SMA rod per each couple is heated), a total power of 8 tabs × 28.7 W = 230 W is required. However, it is worth noting that this estimate is very conservative. In fact, the declared power per unit surface refers to a heater temperature of 400 °C (almost two times the needed one).

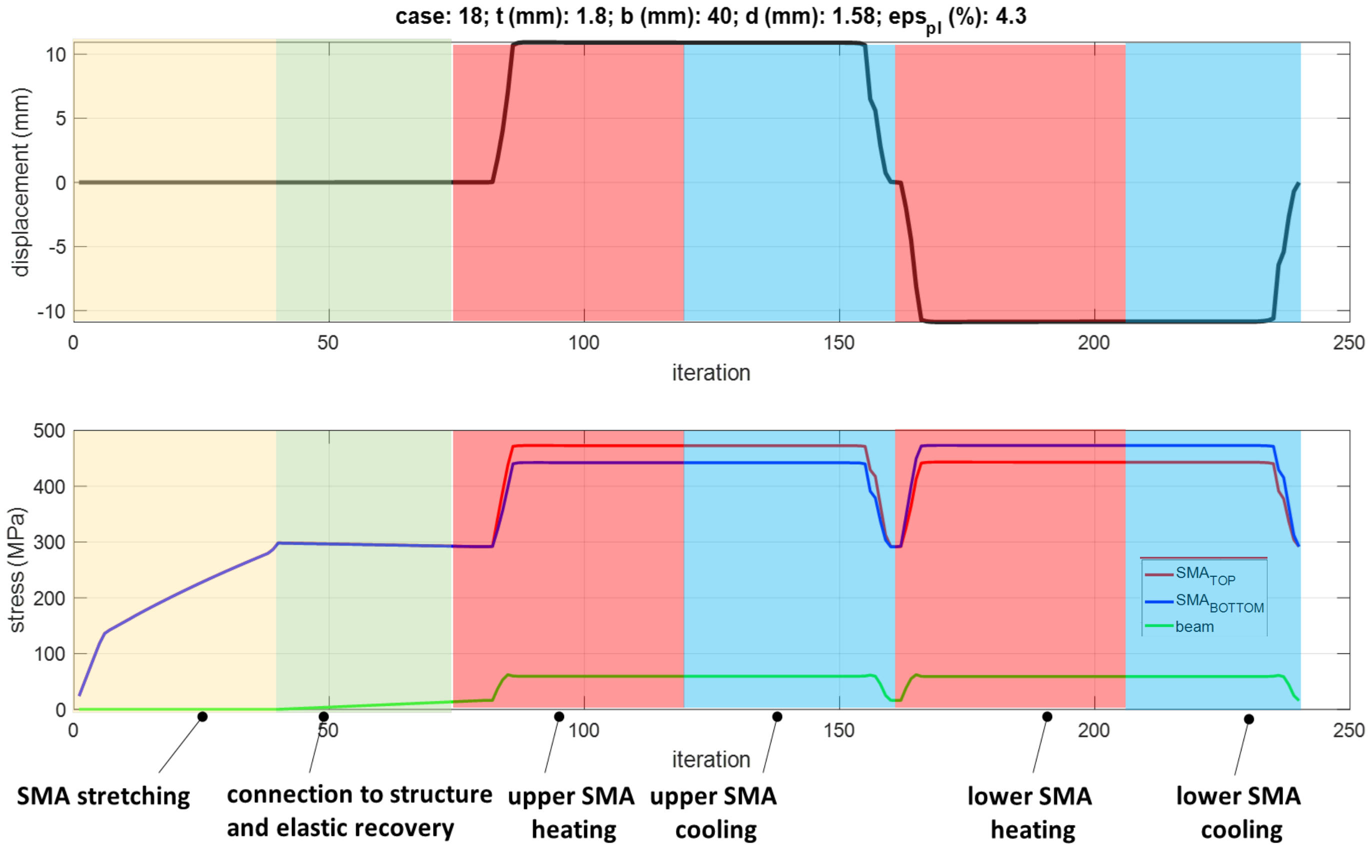

Figure 14. Tip displacement (**top**) and von Mises stress in the beam and in the SMA rods (**bottom**) vs. iteration step.

6. Conclusions

Flexible morphing deployable aeroshells are increasingly emerging as novel and alternative concepts for the controlled re-entry and precise landing of space vehicles. In this work, a preliminary conceptual analysis of a novel shape-changing concept that can be packaged with an off-the-shelf 12U CubeSat was addressed. The deployment mechanism was controlled by a single translational actuator that dictated the overall deployment of the mechanism and, once deployed, the aeroshell shape could be adapted via an SMA-based actuation. Strain recovery in the SMA actuators were a result of thermally induced transformations that underwent against an external force. Such a strain recovery was converted into bending for the individual tabs by contributing to the aeroshell shape changes. Multi-body analyses and preliminary structural parametrization of SMA rods have provided guidelines and potential constraints for an actual implementation of the concept. A maximum of eight ribs was chosen to ensure maximum shape accuracy, allowing the aeroshell to decelerate through entry. After investigating the behavior of the mechanism through a multibody model, it was found that the system deployment is strongly dependent on the components' geometry, hinges' positions, and assembly. Deploying high-precision geometry could enable guidance maneuvers to be carried out by the individual control of morphing flaps providing enhanced versatility, which was otherwise not achievable with the current rigid decelerators. Such a controlled deployment and retraction of the system can provide also an appealing feature in view of repeatable and reliable testing.

The use of an SMA material for actuation, due to the thermal inertia of the material, certainly limits the proposed concept to a low-frequency band, which is, however, compatible for the proposed employment (landing phases). As a next step, further analyses involving both the evaluation of thermal and aerodynamic loads and the assessment of the aeroelastic stability will be assessed, along with possible control strategies driving the systems to minimize the differences between the actual trajectories detected by on board instrumentation and the nominal ones. Once full aerostructural analysis and numerical validation of the small-scale model is achieved, a demonstrator of a morphing aeroshell will be fabricated at CIRA for functional testing.

Author Contributions: Conceptualization, I.D. and C.V.; methodology, I.D., S.A., W.R.S. and C.V.; software, I.D. and C.V.; validation, I.D. and C.V.; formal analysis, I.D., S.A. and W.R.S.; investigation, I.D. and C.V.; resources, I.D. and C.V.; data curation, I.D. and C.V.; writing—original draft preparation, I.D.; writing—review and editing, I.D., C.V. and A.C.; visualization, I.D.; supervision, I.D.; project administration, I.D. and C.V.; funding acquisition, I.D. and C.V. All authors have read and agreed to the published version of the manuscript.

Funding: This research is funded in part by a grant (PGR10074) from the Italian Ministry of Foreign Affairs and International Cooperation (MAECI) in the framework of the first Executive Programme for Scientific and Technological Cooperation between the Government of the Italian Republic and the Government of the federal Republic of Brazil.

Institutional Review Board Statement: Not applicable.

Data Availability Statement: Not applicable.

Acknowledgments: The authors would like to acknowledge F. Naro, the Scientific Attaché at Embassy of Italy in Brazil, for his guidance throughout the execution of the SPLASH project.

Conflicts of Interest: The authors declare no conflict of interest.

References

1. Akin, D. Applications of ultra-low ballistic coefficient entry vehicles to existing and future space missions. In Proceedings of the SpaceOps 2010 Conference Delivering on the Dream Hosted by NASA Marshall Space Flight Center and Organized by AIAA, Huntsvillem, AL, USA, 25–30 April 2010; p. 1928.
2. Smith, B.; Cassell, A.; Kruger, C.; Venkatapathy, E.; Kazemba, C.; Simonis, K. Nano-ADEPT: An Entry System for Secondary Payloads. In Proceedings of the 2015 IEEE Aerospace Conference, Big Sky, MT, USA, 7–14 March 2015; pp. 1–11.
3. Carandente, V.; Elia, G.; Savino, R. Conceptual design of de-orbit and re-entry modules for standard cubesats. In Proceedings of the 2nd IAA Conference on University Satellite Missions and Cubesat Work-shop, Rome, Italy, 3–9 February 2013; pp. 4–7.
4. Esper, J. Cubesat Application for Planetary Entry (CAPE) Missions: Micro-Return Capsule (MIRCA). In Proceedings of the 30th Annual AIAA/USU Conference on Small Satellites, SSC16-XII-05, Toulouse, France, 27–30 September 2016.
5. Hughes, S.; Bailet, G.; Miller, N.; Korzun, A.; Zumwalt, C.; Cheatwood, F. Low Cost Innovative Atmospheric Entry Probes Combining CubeSat and HIAD Technologies. In Proceedings of the International Planetary Probe Workshop-13, Laurel, MD, USA, 13–17 June 2016.
6. Carandente, V.; Savino, R. New Concepts of Deployable De-Orbit and Re-Entry Systems for CubeSat Miniaturized Satellites. *Recent Pat. Eng.* **2014**, *8*, 2–12. [CrossRef]
7. Savino, R.; Aurigemma, R.; Aversana, P.D.; Gramiccia, L.; Longo, J.; Maraffa, L.; Punzo, F.; Scolamiero, L. European Sounding Rocket Experiment on Hypersonic Deployable Re-Entry Demonstrator Background of the Project. In Proceedings of the 8th European Symposium on Aerothermodynamics for Space Vehicles, Lisbon, Portugal, 2–7 March 2015.
8. Jurewicz, D.; Brown, G.; Gilles, B.; Taylor, A.; Sinclair, R.; Tutt, B.; Lichodziejewski, D.; Kelley, C.; Hughes, S. Design and Development of Inflatable Aeroshell Structure for IRVE-3. In Proceedings of the 21st AIAA Aerodynamic Decelerator Systems Technology Conference and Seminar, Dublin, Ireland, 23–26 May 2011. AIAA Paper 2011-2522.
9. Peacocke, L.; Bruce, P.J.K.; Santer, M. Coupled Aerostructural Modeling of Deployable Aerodecelerators for Mars Entry. *J. Spacecr. Rocket.* **2019**, *56*, 1221–1230. [CrossRef]
10. Gardi, R.; Fedele, A.; Pezzella, G.; Vernillo, P.; Savino, R.; Mungiguerra, S.; Dell'Aversana, P.; Gramiccia, L.; Henriksson, K.; Smith, J. Mini-irene: Design of deployable heat shield capsule for a sounding rocket flight experiment. In Proceedings of the 68th International Astronautical Congress, Adelaide, SA, Australia, 25–29 September 2017.
11. Vernillo, P.; Fedele, A.; Gardi, R.; Savino, R.; Punzo, F.; Gunnar, F.; Molina, R. Mini-irene: The first European flight experiment of a deployable heat shield. In Proceedings of the 23rd ESA Symposium on European Rocket and Balloon Programmes and Related Research, Visby, Sweden, 11–15 June 2017.
12. Dutta, S.; Smith, B.; Prabhu, D.; Venkatapathy, E. Mission sizing and trade studies for low ballistic coefficient entry systems to Venus. In Proceedings of the 2012 IEEE Aerospace Conference, Big Sky, MT, USA, 3–10 March 2012; pp. 1–14. [CrossRef]

13. Cassell, A.; Smith, B.P.; Wercinski, P.F.; Ghassemieh, S.M.; Hibbard, K.E.; Nelessen, A.P.; Cutts, J.A. ADEPT, A Mechanically Deployable Re-Entry Vehicle System, Enabling Interplanetary CubeSat and Small Satellite Missions, SSC18-XII-08. In Proceedings of the 32nd Annual AIAA/USU Conference on Small Satellites, Logan, UT, USA, 4–9 August 2018.
14. Venkatapathy, E.; Hamm, K.; Fernandez, I.; Arnold, J.; Kinney, D.; Laub, B.; Andrews, D. Adaptive Deployable Entry and Placement Technology (ADEPT): A Feasibility Study for Human Missions to Mars. In Proceedings of the 21st AIAA Aerodynamic Decelerator Systems Technology Conference and Seminar, Dublin, Ireland, 23–26 May 2011. AIAA Paper No. 2011–2608.
15. Cassell, A.; Brivkalns, C.; Bowles, J.; Garcia, J.; Kinney, D.; Wercinski, P.; Cianciolo, A.; Polsgrove, T. Human Mars Mission Design Study Utilizing the Adaptive Deployable Entry and Placement Technology. In Proceedings of the 2017 IEEE Aerospace Conference, Big Sky, MT, USA, 4–11 March 2017. [CrossRef]
16. O' Driscoll, D.; Bruce, P.J.; Santer, M.J. Origami-based TPS Folding Concept for Deployable Mars Entry Vehicles, AIAA 2020-1897. In Proceedings of the AIAA Scitech 2020 Forum, Orlando, FL, USA, 6–10 January 2020.
17. Green, J.S.; Dunn, B.; Lindberg, R. Morphing Hypersonic Inflatable Aerodynamic Decelerator AIAA 2013-1256. In Proceedings of the AIAA Aerodynamic Decelerator Systems (ADS) Conference, Daytona Beach, FL, USA, 25–28 March 2013.
18. Green, J.S. Morphing Hypersonic Inflatable Aerodynamic Decelerator. In *Thesis Mechanical and Aerospace Engineering*; University of Virginia: Charlottesville, VA, USA, 2012; Available online: https://libra2.lib.virginia.edu/downloads/q811kj77c?filename=Morphing_Hypersonic_Inflatable_Aerodynamic_Decelerator_-_Justin_S_Green.pdf (accessed on 15 February 2023).
19. Fedele, A.; Carannante, S.; Grassi, M.; Savino, R. Aerodynamic control system for a deployable re-entry capsule. *Acta Astronaut* **2021**, *181*, 707–716. [CrossRef]
20. Fedele, A.; Omar, S.; Cantoni, S.; Savino, R.; Bevilacqua, R. Precise re-entry and landing of propellantless spacecraft. *Adv. Space Res.* **2021**, *68*, 4336–4358. [CrossRef]
21. Omar, S.; Bevilacqua, R. Guidance, navigation, and control solutions for spacecraft re-entry point targeting using aerodynamic drag. *Acta Astronaut.* **2019**, *155*, 389–405. [CrossRef]
22. Carna, S.F.R.; Omar, S.; Guglielmo, D.; Bevilacqua, R. Safety analysis for shallow controlled re-entries through reduced order modeling and inputs' statistics method. *Acta Astronaut.* **2019**, *155*, 426–447. [CrossRef]
23. Savino, R.; Carandente, V. Aerothermodynamic and feasibility study of a deployable aerobraking re-entry capsule. *Fluid Dyn. Mater. Process.* **2012**, *8*, 453–477.
24. Fedele, A. A Deployable Aerobraking System for Atmospheric Reentry. Ph.D. Thesis, Industrial Engineering, University of Florida, Gainesville, FL, USA, 2020. [CrossRef]
25. Vanhamel, J.; Eaton, N.; Spreij, R. Using fiber bragg gratings for shape monitoring and adjustment of a thermal protection system aboard a targeted re-entry cubesat. In Proceedings of the 2nd International Conference on Flight Vehicles, Aerothermodynamics and Re-entry Missions Engineering (FAR), Heilbronn, Germany, 19–23 June 2022.
26. Chin, A.; Coelho, R.; Nugent, R.; Munakata, R.; Puig-Suari, J. The CubeSat: The Picosatellite Standard for Research and Education. In Proceedings of the AIAA SPACE Conference & Exposition, San Diego, CA, USA, 9–11 September 2008.
27. Toorian, A.; Diaz, K.; Lee, S. The CubeSat Approach to Space Access. In Proceedings of the IEEE Aerospace Conference, Big Sky, MT, USA, 1–8 March 2008.
28. Tauber, M.E. *A Review of High-Speed, Convective, Heat-Transfer Computation Method*; National Aeronautics and Space Administration Office of Management, Scientific and Technical Information Division: Washington, DC, USA, 1989; NASA Technical Paper 2914. Available online: https://ntrs.nasa.gov/api/citations/19890017745/downloads/19890017745.pdf (accessed on 14 February 2023).
29. Pecora, R.; Amoroso, F.; Magnifico, M.; Dimino, I.; Concilio, A. KRISTINA: Kinematic rib-based structural system for innovative adaptive trailing edge. In Proceedings of the SPIE—The International Society for Optical Engineering, Las Vegas, NV, USA, 20–24 March 2016; Volume 9801, p. 980107.
30. Pecora, R.; Dimino, I. SMA for Aeronautics. In *Shape Memory Alloy Engineering: For Aerospace, Structural and Biomedical Applications*; Elsevier Ltd.: Amsterdam, The Netherlands, 2015; pp. 275–304.
31. Song, S.H.; Lee, J.Y.; Rodrigue, H.; Choi, I.S.; Kang, Y.J.; Ahn, S.H. 35 Hz shape memory alloy actuator with bending-twisting mode. *Sci. Rep.* **2016**, *6*, 1–13. [CrossRef] [PubMed]
32. Sunjai Nakshatharan, S.; Dhanalakshmi, K.; Josephine Selvarani Ruth, D. Effect of stress on bandwidth of antagonistic shape memory alloy actuators. *J. Intell. Mater. Syst. Struct.* **2016**, *27*, 153–165. [CrossRef]
33. Watlow Website. Available online: https://www.watlow.it/products/heaters/watrod-electric-tubular-heaters.cfm (accessed on 2 February 2023).